A&A 482, 279–292 (2008)
DOI: 10.1051/0004-6361:20078699

Astronomy & Astrophysics

First disk-resolved millimeter observations of Io's surface and SO_2 atmosphere⋆

A. Moullet[1], E. Lellouch[1], R. Moreno[1], M. A. Gurwell[2], and C. Moore[3]

[1] LESIA-Observatoire de Paris, 5 place J. Janssen, 92195 Meudon, France
e-mail: arielle.moullet@obspm.fr
[2] Harvard-Smithsonian Center for Astrophysics, Cambrige, MA 02138, USA
[3] The University of Texas at Austin, TX 78712, USA

Received 18 September 2007 / Accepted 3 December 2007

ABSTRACT

Aims. In spite of considerable progress in the last two decades, Io's atmosphere remains poorly understood. The goal of this work is to improve our understanding of its spatial distribution, temperature and dynamics.
Methods. We present millimeter observations of Io's surface and SO_2 atmosphere at 1.4 mm obtained with the IRAM Plateau de Bure Interferometer in January−February 2005. With a synthesized beam of 0.5 × 1.5″, these observations resolve Io's ∼1.0″ disk in the longitudinal / local time direction, and sample the leading and trailing hemispheres of Io.
Results. The measured continuum total flux and visibilities show that continuum radiation originates from a depth of at least 1 cm in Io's subsurface. On both the leading and trailing sides, emission in the SO_2 216.643 GHz line appears spatially narrower than the continuum, and suggests that the atmosphere covers ∼80% of the surface on the leading side and ∼60% on the trailing. On the leading side, disk-resolved spectra yield Doppler shift measurements, indicating a beam-integrated limb-to-limb velocity difference of 330 ± 100 m/s in the prograde direction. Such a flow allows an improved fit of disk-averaged SO_2 spectra, but its origin remains to be understood. Mean gas temperatures are in the range 130−180 K, in agreement with estimates from IR measurements, and with a tendency for higher trailing vs leading side gas temperatures. On the basis of realistic plume models, we find that the contribution of isolated volcanic plumes to the SO_2 emission is small.

Key words. techniques: interferometric – planets and satellites: individual: Io

1. Introduction

In the last 15 years, observations at millimeter, ultraviolet, and infrared wavelengths have revealed that Io's atmosphere is one of the most unusual in the Solar System. Io's atmosphere features a unique composition, dominated by SO_2 and including SO, NaCl, S_2 and several atomic species, ultimately reflecting chemical and atmospheric processing of volcanically-produced gases. It is one of the most tenuous atmospheres (typical pressure ∼1 nbar), and its structure is unique, apparently exhibiting large horizontal variations of density with longitude, latitude, and presumably local time. This variability must be related to the distribution of volcanic (gas plumes) and sublimation (SO_2 frost) sources and condensation sinks. Evidence for temporal variations is also present. Io's atmosphere is also the main source of material to Jupiter's magnetosphere with which it exchanges matter and energy through atmospheric escape and plasma bombardment and heating. Recent reviews on Io's atmosphere and interaction with the plasma torus can be found in McGrath et al. (2004) and Lellouch et al. (2006).

While the above general features seem to be reasonably well established, many key issues are unresolved. There remain uncertainties by factors of several in the mean SO_2 column densities and in the areal extent of the atmosphere. The characteristic atmospheric temperature and its vertical structure are poorly constrained, with gas temperatures in the range 100−600 K claimed from different datasets (e.g. Lellouch et al. 1992; Jessup et al. 2004; Spencer et al. 2005). Several classes of models have been developed to describe the dynamical behavior of Io's atmosphere, including "meteorological" models (global and local, Ingersoll et al. 1985; Ingersoll 1989; Moreno et al. 1991), "unified" models coupling the effect of plasma interaction, horizontal transport, and chemistry on the overall distribution of the atmosphere (e.g. Smyth & Wong 2004, and references therein), and "plume atmosphere" models (e.g. Zhang et al. 2004) studying the evolution of dense gas and dust plumes in various environments. Most of the models predict gas flows from dense to tenuous regions, in particular from the dayside to the nightside and away from volcanic plumes. Although the structure of visible (dust) plumes provides useful constraints, the dynamics of Io's gas atmosphere have never been measured directly, due to the lack of spectral and/or spatial resolution (Geissler & Goldstein 2006). As a consequence, the relative roles of volcanism and sublimation equilibrium in controlling the atmosphere remain uncertain, and arguments have been given in each direction (e.g. Spencer et al. 2005; Lellouch et al. 2006; Saur & Strobel 2004). Active volcanism is the ultimate source of Io's atmosphere, yet the question of its immediate source remains highly significant, in terms of vertical structure, lifetime, composition, and response to insolation variations (e.g. diurnal and eclipse). Along with other techniques, millimeter-wave observations play an important role in characterizing Io's atmosphere. Their specific contributions come from (i) the fact that they sample thermal emission in local thermodynamical equilibrium (LTE) conditions and are therefore directly, and in a simple manner, sensitive to gas temperatures; (ii) their high spectral

⋆ Appendix A is only available in electronic form at http://www.aanda.org

Table 1. Physical observation parameters.

Target	Date	Observed CML (°W)	Apparent diameter (″)
Io	28/01/2005	60–112	0.998
Io	05/02/2005	249–310	1.024

resolution, allowing one, in principle, to measure gas velocities from Doppler-shift measurements; (iii) their high sensitivity to some gases (i.e. SO and NaCl) which are difficult to observe in other wavelength ranges. However, past millimeter-wave observations (primarily obtained with the IRAM 30-m telescope) were limited by poor spatial resolution (~10″), providing only disk-integrated information.

In this paper, we present the first disk-resolved millimeter observations of Io, obtained with the IRAM Plateau de Bure Interferometer (PdBI). Section 2 describes the data acquisition and reduction. Section 3 presents the analysis of continuum data, and implications for the emission properties of Io's surface. Section 4 describes the spectral and spatial characteristics of the SO_2 line emission, and presents complementary IRAM-30 m disk-averaged observations. In Sect. 5, data from both observatories are modeled in the framework of a hydrostatic atmosphere model, meant to represent a sublimation equilibrium atmosphere, by using newly proposed SO_2 distributions (Spencer et al. 2005; Feaga 2005; Feaga et al. 2008). Section 6 describes an initial approach for evaluating in a realistic way the contribution of volcanic plumes. Results are summarized and discussed in Sect. 7.

2. Observations and data reduction

Observations of Io were performed using the IRAM Plateau de Bure Interferometer, a facility consisting of six 15-m diameter antennas (Guilloteau et al. 1992). In order to minimize the contribution of Jupiter in the telescope primary beams (~22″ at 220 GHz), Io must be observed near its maximum eastern (leading side, Io central longitude ~90° W) or western (trailing side, Io central longitude ~270° W) elongation. Observations were obtained on January 28 (leading side), and February 5 (trailing side), 2005 (see Table 1). The array was arranged in the most extended configuration available at that time, with a maximum baseline length of 400 m in the E-W direction. At 1.4 mm and for the low declination of Io at the time of the observations (~−6°), the array provided a highly elongated synthesized beam of ~0.5 × 1.5″, whose long-axis was roughly aligned with Io's pole axis (−20° angle for the leading side observation, −15° for the trailing side observation). Therefore Io (typical diameter of ~1.0″) was resolved primarily in the longitudinal / local time direction.

The primary target line was the 216.643 GHz rotational line of SO_2, one of the strong SO_2 lines previously detected with the IRAM-30 m (e.g. Lellouch 1996). We used a variety of spectral backends, including a 40-kHz (55 m/s at 217 GHz) resolution correlator, well suited to resolve the ~650 m/s SO_2 linewidth, and two 640-MHz broad continuum backends dedicated to measure Io's continuum surface emission simultaneously at 1.3 mm and 3 mm. Weather conditions were good, with 217 GHz system temperatures T_{sys} of ~400 K on Jan. 28 and ~350 K on Feb. 5.

The PdBI receivers were at that time double sideband, with a band separation of 3 GHz, allowing us to simultaneously search for the SO 219.949 GHz line, previously observed on Io (Lellouch et al. 1996). However, SO was not detected in our observations. As the presence of SO in Io's atmosphere may result from thermochemical equilibrium in volcanic plumes (Zolotov & Fegley 1998), this may be a consequence of temporal variability. This is supported by recent IR observations of Io in eclipse (Laver et al. 2007) which indicate that SO 1.7 μm emission shows variation with time by a relative factor of 3. On each date, observations lasted about 7 h, over which Io rotated by 50–60°. About half of the observing time (3.3 h on the leading side and 3.6 h on the trailing) corresponded to on-source measurements. The rest of the available time was spent in frequent (every 20 min) pointing and focus measurements and calibration. For phase, amplitude and bandpass calibrations, we used the strong quasi-point sources 3C 273 and MWC 349. For absolute flux calibration, we observed continuum emission from Ganymede and Callisto, providing an estimated absolute accuracy of ~5% (see below and in online material). A 22 GHz radiometer was used to monitor atmospheric phase variations. Due to high wind (>10 m/s, unsuitable for proper tracking), the observations acquired near the end of the first period were discarded, leading to an effective on-source time of only 2.5 h on the leading side.

Data reduction, including corrections and calibrations, was performed under the CLIC environment of the GILDAS package (`www.iram.es/IRAMFR/GILDAS`). Bandpass calibration indicates variations of amplitude and phase by ~2% and ~1.5° respectively over the bandwidth. Phase and amplitude rms at 217 GHz were 35° and 12% on the leading side and 12° and 6% on the trailing side. The variations of amplitude and phase with time are due to atmospheric de-correlation, and to pointing and focus errors. For the leading side observations, the 1-σ sensitivity is 1.7 mJy/beam on the continuum ($\delta\nu$ = 640 MHz), 60 mJy/beam on the integrated linewidth (600 KHz), and 230 mJy/beam per spectral channel (40 kHz). On the trailing side, these figures are about 35% lower (1.1, 39, and 150 mJy/beam, respectively), primarily due to increased integration time and better weather conditions.

3. Continuum analysis and modeling

The measured continuum emission is thermal radiation from Io's surface/subsurface. Calibrated interferometric visibilities in the 1.4 mm continuum are displayed in amplitude for the leading and trailing side observations in Fig. 1. Each of these visibilities corresponds to 1 min of integration. We performed similar continuum measurements of Ganymede (leading side) and Callisto (lead and trail), that we used as absolute flux calibrators. See online material for details on the calibration process. For Io, we found brightness temperatures of 93 K on the leading side and 99 K on the trailing at 1.4 mm. Although all measurements are affected by a 5% absolute uncertainty, the relative variation of the brightness temperatures between the two sides is well determined on both wavelengths since we are using the same absolute calibrator: the leading side emission is ~5% colder than the trailing side. Io's leading side is on average brighter than the trailing side, by about 10% (McEwen 1988). However, with a mean Bond albedo of 0.52 (Simonelli et al. 2001), this should lead to a difference in surface temperature of only ~3%. A possible additional effect is that the material of the leading side is more porous than on the trailing side (Domingue et al. 1998), possibly causing millimeter-wave radiation to come from deeper (and hence colder) subsurface levels.

As shown in Fig. 1, a uniformly emitting disk model provides a satisfactory fit of the continuum visibilities on both the leading and trailing sides. This behavior is not expected given

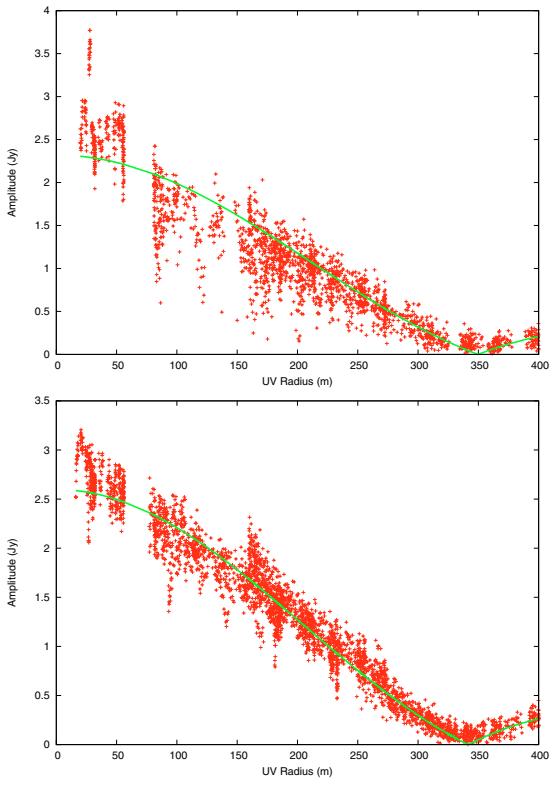

Fig. 1. Continuum visibilities (crosses) and uniform brightness temperature models (line). *Top*: leading side. *Bottom*: trailing side.

the existence of large surface temperature variations at Io, especially diurnal and latitudinal, and the fact that the surface emissivity may in principle strongly vary with emission angle, if the surface is characterized by a radio dielectric constant significantly larger than unity. We further investigated these aspects using physical modeling of the trailing side continuum data. On the leading side, the quality of the data, being affected by a relatively large phase rms (35°), is not sufficient for distinguishing between surface models.

Our surface emission model includes:

- a model of the distribution of physical surface temperatures. Surface temperatures on Io result from the combination of solar and internal heating. Veeder et al. (1994) estimate that both components contribute comparable amounts to the total thermal emission from Io. We considered two kinds of surface temperature models. In the first one, following the description of Wong & Smyth (2000) based on the model of Kerton et al. (1996), the local surface temperature is assumed to vary as $T_{\rm surf} = B(\cos({\rm SZA}))^{0.75} + A$, where SZA is the solar zenith angle, A is the terminator surface temperature and B is the temperature variation across the illuminated disk. Large horizontal surface temperature variations will cause the effective emission size to decrease. The second surface temperature model we tested was the one used by Spencer et al. (2005) (their Fig. 4), which matches 27 μm Galileo/PPR data. This model shows smooth surface temperature variations from ~85 K at the terminator and in polar regions to ~133 K at subsolar longitude, with a mean surface temperature of 118 K. As discussed later, we also considered subsurface temperature models.
- a description of the emitting properties of the surface. We used a classical description of the surface emissivity, based on Fresnel's law of reflection for the average of the two polarizations, with the dielectric constant ϵ as a free parameter (see e.g. Muhleman & Berge 1991). A large value of ϵ decreases the disk-average surface emissivity e and therefore the mean brightness temperature, since in the Rayleigh-Jeans limit $T_{\rm B} = eT_{\rm physical}$. In addition, by preferentially decreasing the emissivity at large emission angles, it reduces the effective emission size. This effect can be reduced if surface roughness effects are important (e.g. Rudy et al. 1987).

For any combination of surface temperature distribution and emission properties, we computed the local brightness temperatures on a very fine (0.008″ mesh) grid. Total flux and individual visibilities corresponding to the u, v coverage of the observations were then calculated within the GILDAS environment and compared with the observed values, focusing on the u, v radius range near zero-crossing. Since Io's disk is resolved in the longitudinal direction, the zero-crossing range is diagnostic of the characteristic emission size in that direction. To facilitate comparison, observed and modeled visibilities were averaged radially by bins of 5 m.

For the surface temperature distribution of Spencer et al. (2005), a disk-average brightness temperature of 93−99 K implies a mean emissivity of 0.79−0.84. This value is consistent with inferences by Muhleman & Berge (1991) who measured (at 2.6 mm) a brightness temperature of 101 ± 9 K for a disk-averaged physical temperature of 119 K. For a Fresnel emissivity law and surface sounding, the emissivity we determine would require a dielectric constant of ~4. This is much higher than typical values for Mars or the Moon (ϵ = 2−2.5), but might not be unreasonable for an icy surface (e.g. water ice has a dielectric constant of 3.1). However, as demonstrated in Fig. 2, even if the emissivity is constant with emission angle, a brightness temperature following the Spencer et al. (2005) distribution is inconsistent with the data, as it leads to a zero-crossing radius larger than observed, i.e. too small a characteristic emission size in the longitudinal direction. In fact, at λ = 1.4 mm, the zero-crossing radius for a uniform disk of Io's apparent size (the largest possible model) is 339.8 m, fully consistent with the observed value of 340 ± 2 m. This stringent constraint means that Io's brightness temperature is essentially uniform in the longitudinal direction best probed by our observations. Assuming again an emissivity independent of emission angle, a model in the form $T_{\rm surf} = B(\cos({\rm SZA}))^{0.75} + A$ is consistent with the data only for $B < 10$, i.e. if the brightness temperature varies by less than ~10% with longitude. Conversely, even assuming a spatially uniform *physical* temperature, the data would rule out a Fresnel-type variation of the emissivity for a dielectric constant larger than ~1.1.

This surprising result does not account for the presence of surface roughness, which has the effect of attenuating the variation of emissivity with emission angle. We found that for a more typical ϵ = 2−2.5 value and a constant physical temperature, a Fresnel-like emission model can be consistent with the data provided that the roughness, as defined by the mean rms slope angle, is at least equal to 40° (Fig. 2). This value may seem large, given that Io's surface is photometrically only moderately rough (photometric roughness ~25°, Simonelli et al. 1998). We note however that the mean slope angle, as derived from thermal-IR observations, is 27°−35° for the Moon (Spencer 1990; Winter & Krupp 1971; Vogler et al. 1991) and 20° for Mercury (Emery et al. 1998). At radio wavelengths, Mitchell & de Pater (1994) find rms slopes of ~10° for the Moon longwards of λ = 2 cm, but ~35° at λ = 0.8 cm, while the photometric roughness of the Moon is ~21°, showing that the photometric roughness is not a

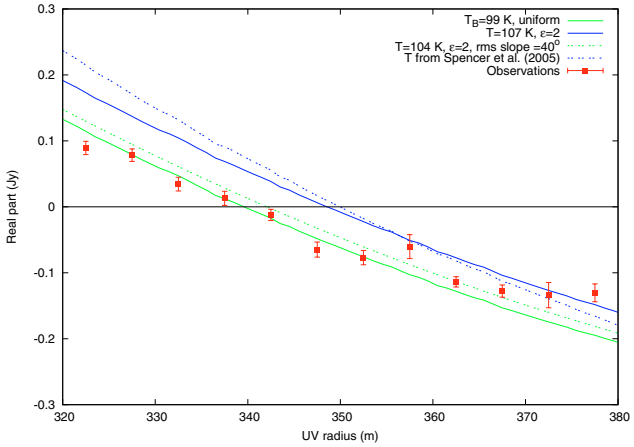

Fig. 2. Real part of trailing side continuum visibilities near zero-crossing, compared to various models. See text for details.

direct indicator of the thermal roughness. If we were still to assume for Io a 1.4 mm roughness of 25°, our observations would imply a maximum $\epsilon = 1.4$ dielectric constant.

The low value of the global emissivity and the uniformity of the brightness temperatures with longitude/local time strongly suggest that millimeter-wave continuum emission probes Io's subsurface layers. Veeder et al. (1994) indicate that Io's surface temperatures result from equilibrium with volcanic and passive components, the latter being well modeled as a combination of a high-albedo, infinite thermal inertia unit, and a lower-albedo, zero thermal inertia unit. The Spencer et al. (2005) surface temperatures clearly show the diurnal variations associated with the second unit. Temperatures at depth must be lower and more longitudinally uniform.

We did not attempt here to construct a detailed subsurface temperature model, including the various heat reservoirs. However, we note that in the simplified framework of a surface in equilibrium with solar input only, the equatorial surface temperature profile shown by Spencer et al. (2005) is characteristic of a thermal parameter Θ (as defined by Spencer et al. 1989) in the range 0.5−1.3. For this range of Θ, deep subsurface temperatures are approximately equal to 0.67−0.72 times the subsolar temperature, and averaged over the dayside, the deep subsurface temperature is 0.8 times the average surface temperature. This falls in the range of the observed global emissivity, since the measured brightness temperature is about 95 K while the infrared-measured surface temperature is 118 K (Spencer et al. 2005). In addition, for these values of Θ, longitudinal variations less than 10% occur at distances of at least 10−12 skin depths below the surface, where the skin depth d_s is the characteristic length over which diurnal changes propagate. d_s is related to the thermal parameter Θ through $d_s = \sigma e T_{eq}^3 \Theta/(\Omega \rho c)$ where Ω is Io's rotation rate, c is the specific heat capacity, e is the bolometric emissivity, ρ is the density. Taking $c = 3.5 \times 10^6$ erg g^{-1} K^{-1} (a typical value for regolith and for water ice), $T_{eq} = 142$ K, $\rho = (0.5-1)$ g cm^{-3}, $e = 1$, and a typical $\Theta = 1$, Io's skin depth is estimated to be 1.4−2.7 mm. Our continuum observations thus probe at least 1.4 cm in the subsurface, corresponding to 10 wavelengths. This is consistent with the conclusion of Muhleman & Berge (1991) and is fairly typical of planetary surfaces (for example, radio observations penetrate 12−15 λ in the surface of Mars (Rudy et al. 1987), although some bodies (e.g. Ganymede) show a different behavior, with brightness temperatures longward of ∼1 mm even lower than the deep subsurface temperatures (Muhleman & Berge 1991). In summary, our measurements indicate that the 1.4 mm continuum radiation from Io represents emission from layers 1.5−3 cm below the surface, with an emissivity of 1. Results on Ganymede and Callisto will be presented elsewhere. We note finally that De Pater et al. (1984) obtained VLA measurements of all Galilean satellites at 2 and 6 cm, but, due to S/N limitations, could not study variations of the radio brightness temperature across the disks.

4. SO_2 line emission

The tracking system on-line at PdBI corrects for the topocentric velocity of planets but not for the planetocentric velocity of satellites. Due to the rapid rotation of Io around Jupiter, the line is displaced by many 40 kHz channels over the course of an observation. Velocity corrections were performed in the data reduction phase, by using ephemeris provided by W. Thuillot from IMCCE (see `www.imcce.fr`). In practice, the velocity parameter was changed in each individual scan, and data were resampled on a fixed velocity table before further analysis.

Self-calibration of the data was performed, using the best continuum (i.e. spatially uniform) models previously derived. This technique, which helps to correct atmospheric phase errors by referencing the phase to that expected on the source, is usually applicable on strong continuum sources. Self-calibrated emission in the line channels was then subtracted from the continuum model directly in visibility space, so that the spectra and maps we present pertain to the pure SO_2 line emission. Channel maps were obtained from Fourier transform of the visibilities and subsequent deconvolution with the HOGBOM algorithm (Hogbom & Brouw 1974).

4.1. Line-integrated emission maps

Figure 3 shows SO_2 line emission maps calibrated by the continuum data and integrated over the line width (520 kHz on leading side, 600 kHz on trailing). For easy visualization, maps were rotated so that Io's polar axis is oriented vertically (with North Pole at the top) on the images. A qualitative comparison with the self-calibrated continuum map shown in the same figure suggests that on both sides, the SO_2 emission region is narrower than the continuum. In both maps the emission appears somewhat shifted to the East, especially on the leading side where the significance of the ∼0.2″ displacement is visually estimated to be 2σ. A North displacement is also suggested on the trailing side. In the line-integrated maps of Fig. 3, the contour step corresponds to 50 mJy/beam, and the mean rms is 55 (resp. 45) mJy/beam on the leading (resp. trailing) side. Peak emission is ∼410 mJy/beam on the leading side and ∼275 mJy/beam on the trailing. The total line flux, averaged over the linewidth, is about 1.05 Jy on the leading side and 0.5 Jy on the trailing. This corresponds to brightness temperature contrasts, referenced to Io's disk, of 40 K and 20 K respectively.

Due to the incomplete filling of the *uv* plane, it is preferable to analyze the line-integrated maps in visibility space. This can allow one to retrieve all emission parameters simultaneously (total flux, emission widths in two directions, and RA, Dec position of maximum). To estimate a characteristic size of the emission region, we performed model fits in which the source region was described as either a uniform brightness elliptical disk (D) or an elliptical Gaussian (G).

Results are presented in Table 2. The ellipse orientation parameter retrieved by the fit is close to the direction of the synthesized beam axis, hence the ellipse minor axis size corresponds to

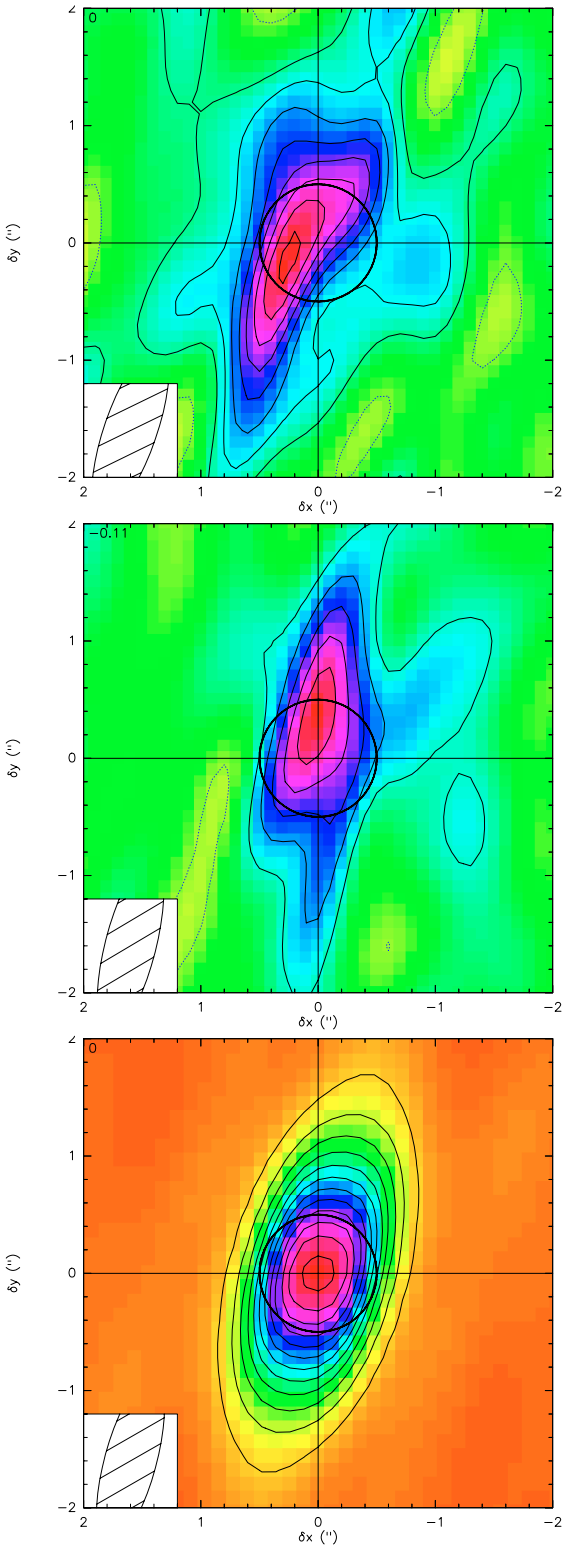

Fig. 3. Maps of SO_2 216.643 GHz line emission and continuum after phase self-calibration. *Top*: leading side line emission. *Center*: trailing side line emission. *Bottom*: continuum map. Contour step is 50 mJy/beam for the line data, 100 mJy/beam for the continuum data. The circle indicates the size of Io. The synthesized beam is shown in the inset.

the best resolved size (in approximately the longitudinal direction). The main result is that the SO_2 emission region appears effectively smaller than the 1.0″ continuum. For a disk model, the resolved emission size is 0.91 ± 0.08″ on the leading side, and 0.66 ± 0.16″ on the trailing. For an elliptical Gaussian model, the resolved size (*FWHM*) is 0.65 ± 0.10″ and 0.44 ± 0.13″ respectively. These figures are to be compared with the *FWHM* of a Gaussian fit of a uniform 1.0″ disk, namely 0.67″. Model fits also confirm that the significance of the sky East (i.e. Io west, or morning) displacement on the leading side emission is only 2-σ. A North-displacement on the trailing side is also measured, but with a very low significance (0.25 ± 0.2″) due to the low spatial resolution in that direction.

Our data provide the first direct measurements (albeit in one direction only) of the characteristic size of the millimeter-line emission from Io. If we assume an atmosphere restricted to ±45° latitude, as indicated by HST Lyα imaging (Feaga 2005) and 2000−3000 Å spectroscopy (Jessup et al. 2004), the longitudinal extent we determine converts to a ∼75−90% atmospheric coverage on the leading side and 45−75% on the trailing. These figures are valid for the elliptical disk models, and similar numbers (82−100% and 45−85%) are found for the Gaussian models. Previous estimates were based on the analysis of single-dish measurements with a beam size (∼10″) much larger than Io (Lellouch et al. 1992, 2006; Lellouch 1996). Based on multiple line observations from IRAM-30 m telescope, and in the framework of a hydrostatic atmosphere model, very localized atmospheres were inferred, covering typically 5−20% of the projected disk in 1991−1994 and 15−40% in 1999−2002 (discussed below). The atmospheric coverage we determine here is considerably larger than the initial estimates and more consistent with the more recent inferences. Noting that Io rotates by 50−60° over the course of an observation, the narrower size of the SO_2 emission compared to the continuum confirms that the atmosphere is longitudinally heterogeneous. With the determined emission sizes, the effective brightness temperature of the emitting area is 137−146 K on the leading side (i.e. 43−53 K higher than the 93 K continuum) and 125−143 K on the trailing side (26−44 K higher than the 99 K continuum) using the uniform disk model.

4.2. Spectrally-resolved maps

Figure 4 shows deconvolved spectral maps of SO_2 on the leading and trailing hemispheres. To improve the visual distinction of the spectra, they are presented with a 0.2″ spatial sampling, and a 120 kHz spectral resolution.

On the trailing side, the emission is weak and lines appear to be detected above the noise only in the vicinity of the central meridian. Thus, the spectral map does not provide information beyond that of the line-integrated map (Fig. 3). In contrast, on the leading side, the S/N is high enough that meaningful Gaussian fits can be obtained at most beam positions, providing maps of the Doppler shifts and line widths (Figs. 6 and 7). Doppler shifts are referenced to a rest frequency of 216.643303 GHz (from Cologne database for infrared spectroscopy `http://www.ph1.uni-koeln.de/vorhersagen/`). This frequency is probably known to within 3 kHz (4 m/s), as inferred from the comparison of several molecular catalogs, including the JPL catalog (Pickett et al. 1998).

Figure 5 shows examples of Gaussian fits for a series of five points separated by 0.2″ along Io's equator. Formal 1-σ uncertainties on the line position and linewidth can be as low as ∼30 m/s. However, errors may also result from the deconvolution process. By testing other deconvolution algorithms and supports, we found that the deconvolution introduces additional uncertainties at the ∼50 m/s and 80 m/s level in the line position

Table 2. Fits of the observed SO_2 emission with elliptical models. G stands for elliptical Gaussian model, D for elliptical disk. The synthesized beam orientation is −20° on the leading side and −15° on the trailing side.

Fit type	Ellipse orientation (°)	Total flux (Jy)	Resolved size (″)	ΔRA (″)	ΔDec (″)
Leading side					
D	–15.6 ± 3.5	1.14 ± 0.11	0.91 ± 0.08	0.18 ± 0.10	–0.03 ± 0.29
G	–15.9 ± 5.7	1.16 ± 0.11	0.65 ± 0.10	0.20 ± 0.10	–0.02 ± 0.27
Trailing side					
D	–5.0 ± 6.9	0.52 ± 0.08	0.66 ± 0.16	0.017 ± 0.05	0.29 ± 0.18
G	–4.9 ± 7.6	0.54 ± 0.09	0.44 ± 0.13	0.026 ± 0.05	0.24 ± 0.19

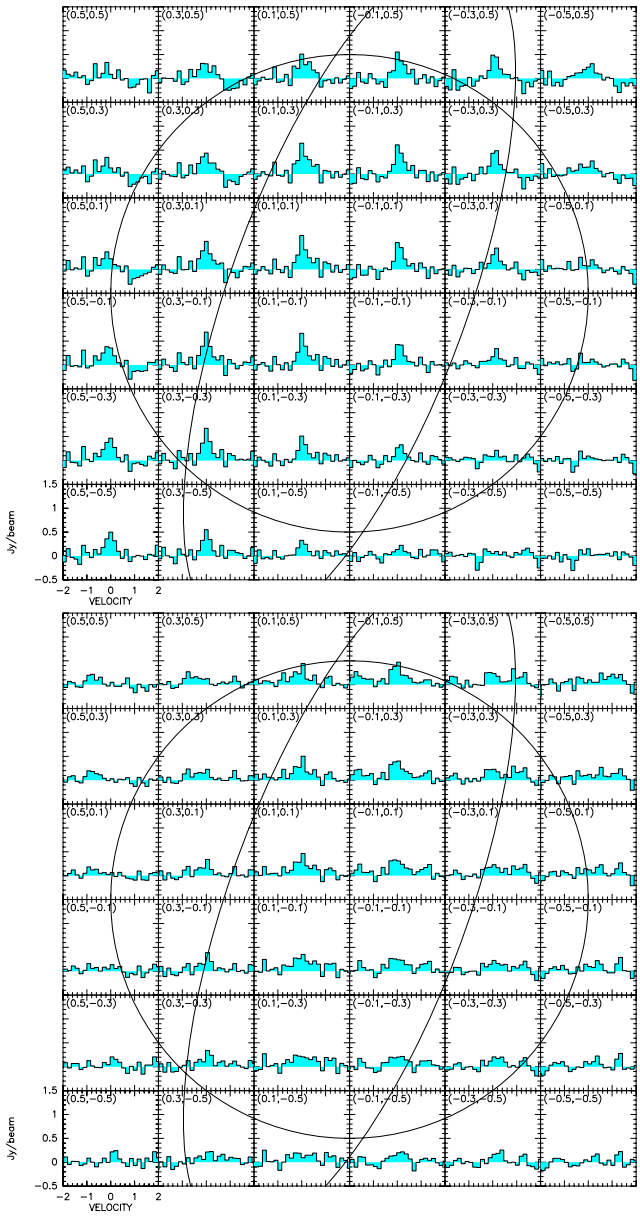

Fig. 4. Spectral maps in the SO_2 line at 216.643 GHz. *Top*: leading size. *Bottom*: trailing side. RA, Dec offsets (in ″) are indicated for each beam position. The spectral resolution is 120 kHz. The surface of Io and the synthesized beam are indicated.

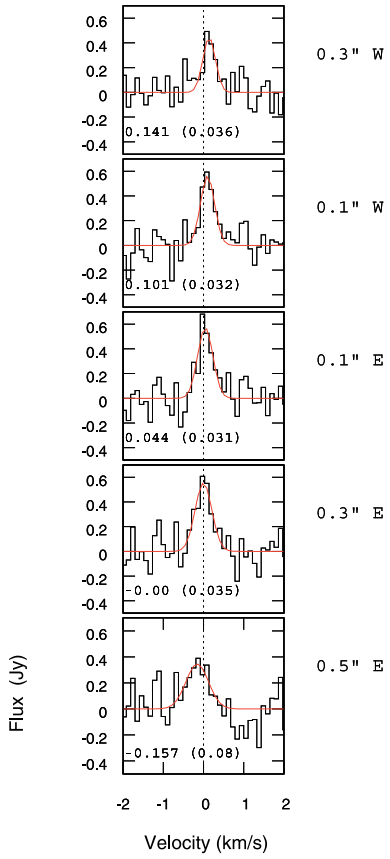

Fig. 5. SO_2 line spectra observed at five beam positions along Io's Equator on Io leading side. Gaussian fits are superimposed and Doppler shifts from rest frequency (km s^{-1}) are indicated, with their 1σ error bar.

and linewidth, respectively. As shown in Figs. 6 and 7, strong redshifts (160 ± 80 m/s) and relatively narrow (*FWHM* = 350 ± 110 m/s) lines are observed on the west limb, while blue-shifted (−170 ± 80 m/s) and somewhat broader lines (600 ± 110 m/s) are present on the east limb. The Doppler shift at disk center is nominally 70 m/s, but its significance is dubious. The resampling procedure adds uncertainties at the level of 1/2 channel, i.e. 27 kHz. When this is combined with the noise level and the ∼50 m/s uncertainty associated with the deconvolution process, the disk center shift may in fact be consistent with zero. We note that similar Doppler shift measurements on Titan obtained with PdBI (Moreno et al. 2005) also indicate unexplained disk center shifts at the level of ±40 m/s. In this situation, relative frequency measurements are much more precise, and the best determined parameter is the limb-to-limb difference in Doppler shift, found to be 330 ± 100 m/s. This is significantly larger than the 75 m/s equatorial solid rotation of Io, and must be the signature of atmospheric dynamics.

A channel-by-channel *uvfit* in visibility space yields the disk-integrated leading side line, which can be calibrated in brightness temperature contrast (ΔT_B) referred to Io's disk. Results are somewhat sensitive to the specified emission size, so we used

Table 3. Gaussian fits of disk-averaged strong lines. Values in parentheses indicate 1-σ error bars.

Date	Lead/Trail	Frequency (GHz)	Amplitude (K)	Shift (km s^{-1})	Width (km s^{-1})
9/10/1999	L	221.965	33.1 (2.1)	–0.034 (0.015)	0.635 (0.048)
25/11/1999	L	216.643	40.6 (1.3)	–0.024 (0.010)	0.664 (0.025)
28/01/2005	L	216.643	45.5 (9.1)	0.016 (0.065)	0.651 (0.065)
10/10/1999	T	221.965	37.4 (1.2)	0.108 (0.011)	0.682 (0.028)
26/11/1999	T	251.199	34.9 (2.0)	0.046 (0.021)	0.724 (0.052)
26/11/1999	T	251.210	23.8 (1.5)	0.052 (0.024)	0.665 (0.065)

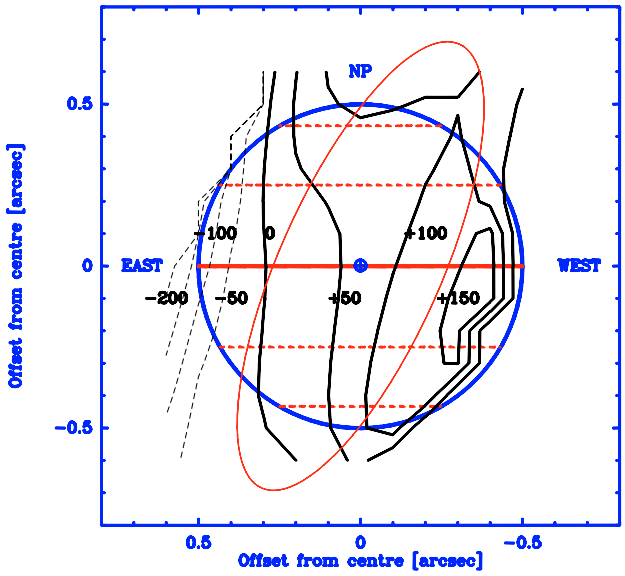

Fig. 6. Map of the Doppler shifts (m/s) on the SO_2 216.643 GHz line on the leading side, from PdBI data. Positive velocities are indicated by solid black lines and negative velocities by dashed black lines. Contour level is 50 m/s.

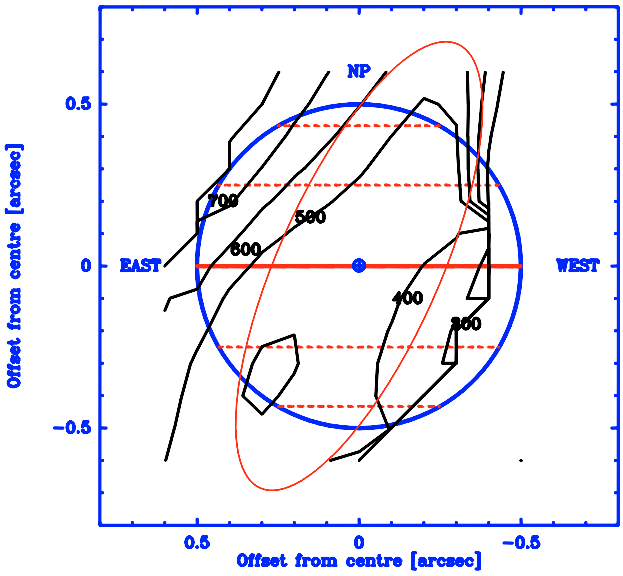

Fig. 7. Map of the 216.643 GHz line width (*FWHM*, in m/s) on the leading side, from PdBI data. Contour level is 100 m/s.

the size and position results previously determined for the integrated line. A Gaussian fit of this line (Table 3) indicates a linewidth of 651 ± 65 m/s. This is larger than most spatially-resolved linewidths (Fig. 7). As expected given the spatially resolved Doppler shifts obtained above, this suggests that the linewidth of disk-integrated lines results, at least partly, from the combination of different gas velocity directions, and not solely from gas temperature and optical depths effects, as originally proposed by Lellouch et al. (1992).

4.3. Single-dish observations

We reanalyzed observations obtained at the IRAM-30 m in Oct.–Nov. 1999. Details on the observational techniques can be found in Lellouch et al. (1992). These observations, which cover four observing nights (two on the leading side and two on the trailing), have been presented in partial form by McGrath et al. (2004) and Lellouch et al. (2006), but were not fully analyzed. Although disk-averaged, their interest is three-fold (i) they are the highest S/N millimeter observations available; (ii) on one occasion (Nov. 25), they include the 216.643 SO_2 GHz line, providing a comparison with the PdBI observations; (iii) on the other three occasions, they consist of multiple SO_2 line observations. The observations on Oct. 9 and 10, 1999, cover three SO_2 lines, at 221.965, 104.239 GHz, and 146.605 GHz, sampling simultaneously a significant range of optical depths (relative opacities at 150–225 K: 1, 0.42, and 0.26). Observations on Nov. 26 include a doublet at 251.199 and 251.210 GHz, with relative opacities of 1.28 and 0.63.

Gaussian fits of the strong 216.643, 221.965, and 251.199 GHz lines are gathered in Table 3. On the leading side, linewidths (649 ± 22 m/s in average) appear fully consistent with the disk-integrated PdBI spectrum, and line contrasts (38 ± 2 K and 46 ± 8 K for 30-m and PdBI data, respectively) are also marginally consistent. Strong lines observed from IRAM-30 m in 1999 have comparable contrasts on the leading and the trailing sides. This differs from the case of the PdBI 2005 observations in which the 216.643 GHz total flux is a factor of two weaker on the trailing side than on the leading. This is most likely due to temporal variations. Monitoring of the strong SO_2 lines from IRAM-30 m has shown that they were at least a factor of 1.5 weaker in 1993–1994 than in 1999 (McGrath et al. 2004), with brightness temperature contrasts of ∼20 K only for the earliest observations.

In what follows, we present models of the IRAM-30 m and PdBI data. We focus on hydrostatic equilibrium models, which are easier to implement, but also attempt to evaluate the contribution of volcanic plumes.

5. Hydrostatic models

We first assume that Io's atmosphere is in hydrostatic equilibrium with the surface. This description is meant to represent a sublimation atmosphere in equilibrium with surface frosts. Because the SO_2 frost distribution (Douté et al. 2001) and surface temperature are not uniform, sublimation equilibrium is expected to induce large horizontal variations of the SO_2 gas

density, in turn producing local and global-scale atmospheric dynamics (Ingersoll et al. 1985; Ingersoll 1989; Moreno et al. 1991; Wong & Johnson 1996). As detailed hereafter, we test horizontally variable SO_2 gas distributions, and assume that locally, the vertical profile of SO_2 can be deduced from its surface density by applying the hydrostatic law with a given (generally isothermal) gas temperature profile. Although the day-to-night flow associated with the large day-to-night pressure gradients may result in significant (up to ~100 m/s) vertical velocities above ~100 km from the surface (Wong & Smyth 2000), we neglect here all vertical motions.

5.1. Code description

Gas emission from Io's atmosphere occurs in local thermodynamical equilibrium (LTE) conditions down to extremely small densities, so that LTE can be safely assumed throughout the atmosphere (Lellouch et al. 1992). To model the SO_2 emission, Io's disk is partitioned in a fine grid of 0.008 arcsec projected resolution, i.e. about 125 points across a diameter. At each point of the grid, characterized by its latitude and longitude, the SO_2 column density is taken a priori from other observations, and the SO_2 density profile as a function of altitude is calculated from hydrostatic equilibrium, under an assumption on the gas temperature (or vertical temperature profile). The radiative transfer is then performed at each point of the grid, accounting for the appropriate airmass, and for the solid-rotation velocity of Io (75 m/s at equator). Calculations are adapted to the precise conditions of observations (see Table 1), including the variation of the central meridian longitude (CML) over the duration of the observations. In practice, since the latter varies by about 50–60°, synthetic spectra are calculated by steps of 10° in CML and averaged.

We considered two SO_2 spatial distributions based on recent observations. The first one is derived from the analysis of HST Lyα images (Feaga 2005; Feaga et al. 2008). SO_2 columns are tabulated with a spatial resolution of 5° × 5°. Maximum column densities of $\sim 5 \times 10^{16}$ cm^{-2} are reached near 140° W and at low latitudes, while densities of $\sim 1 \times 10^{16}$ cm^{-2} are typical of the trailing side. The second proposed distribution is based on disk-integrated thermal IR (19 μm) spectroscopy at multiple orbital longitudes (Spencer et al. 2005). Disk-averaged column densities at each orbital longitude are interpreted through a latitude-dependent model, with SO_2 columns sharply decreasing poleward of 50°. This allows us to reconstruct an approximate 2-D distribution of the SO_2 abundance. The equatorial column density varies strongly with longitude, with a maximum of $\sim 1.5 \times 10^{17}$ cm^{-2} on the anti-jovian hemisphere (210° W) and up to ten times smaller columns in some locations on the trailing hemisphere. On a hemispherically-averaged basis, column densities are a factor 2–3 larger than in the Feaga et al. (2008) model. As explained later, we also considered departures (scaling factors) from these two distributions.

As the mean temperature of Io's atmosphere (and even more the vertical temperature profile) is poorly constrained, the gas temperature was taken as a free parameter, mostly considering isothermal atmospheres for simplicity. In all situations, the gas temperature was assumed to be independent of latitude and longitude. This description is certainly a gross oversimplification of Io's reality, given for example the likely existence of a terminator shock (Austin & Goldstein 2000). Finally, as explained below, we also introduced horizontal wind velocities in the model.

Models in their different forms were compared to the various datasets. For comparison with the IRAM 30-m spectra, synthetic spectra calculated at each grid point are simply spatially averaged. Comparison with the spatially-resolved data obtained at PdBI involves a spatial convolution of the models with the PdBI synthesized beam. In practice, this is best done within the GILDAS mapping environment: from the grid of models, synthetic visibilities are generated with the same u, v sampling as in the observations, and are then deconvolved to produce synthetic images. Models can also be directly analyzed in the u, v plane.

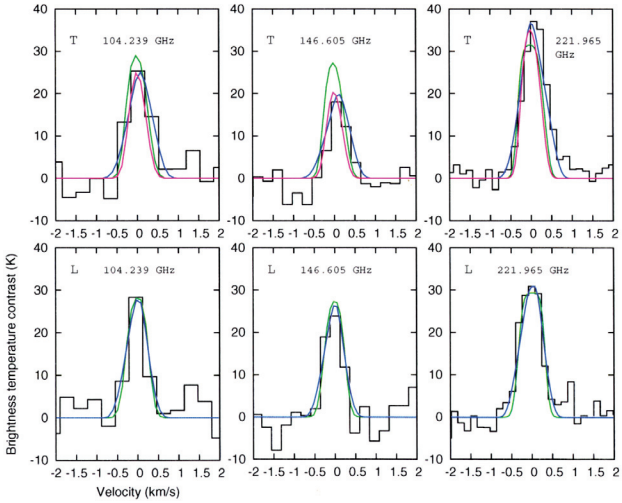

Fig. 8. Fit of IRAM-30 m October 9 (lead, *bottom*) and 10 (trail, *top*), 1999 observations, with models derived from the Spencer et al. (2005) SO_2 distribution. Data are shown as black histograms. Green lines: original Spencer distribution. Pink lines: rescaled Spencer distribution (identical to original on leading side). Blue lines: rescaled distribution, with horizontal winds. See text and Table 4 for details and parameters.

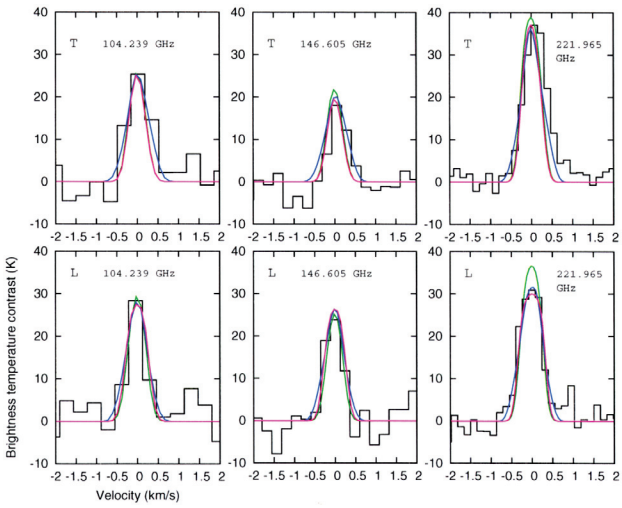

Fig. 9. Fit of IRAM-30 m October 9 (lead, *bottom*) and 10 (trail, *top*), 1999 observations, with models derived from the Feaga et al. (2008) SO_2 distribution. Data are shown as black histograms. Green lines: original Feaga distribution. Pink lines: rescaled Feaga distribution. Blue lines: rescaled distribution, with horizontal winds. See text and Table 4 for details and parameters.

5.2. Fitting the IRAM-30 m data

Figures 8 and 9 show fits of the IRAM-30 m data obtained on Oct. 9 (leading side) and 10 (trailing side), 1999, with models

Table 4. Hydrostatic models solution fits for disk-averaged lines. S and F stand for the Spencer et al. (2005) and Feaga et al. (2008) SO_2 distribution models.

Date	Lead/ Trail	Gas model	Gas temperature (K)	Horizontal wind (m/s)
9/10/1999	L	S	128	0[1]
9/10/1999	L	S	130	180
25/10/1999	L	S	140	0[1]
25/10/1999	L	S	150	270
28/01/2005	L	S	157	0[1]
28/01/2005	L	S	166	200
9/10/1999	L	F	147	0[1]
9/10/1999	L	F x 3	132	0[1]
9/10/1999	L	F x 3	135	170
25/10/1999	L	F x 3	145	0[1]
25/10/1999	L	F x 3	150	200
28/01/2005	L	F x 3	165	0[1]
28/01/2005	L	F x 3	175	200
10/10/1999	T	S	136	0[1]
10/10/1999	T	S x 0.2	150	0[1]
10/10/1999	T	S x 0.4	165	300
26/10/1999	T	S x 0.2	165	0[1]
26/10/1999	T	S x 0.3	175	250
05/02/2005	T	S x 0.4	150	0[1]
05/02/2005	T	S x 0.4	160	200
10/10/1999	T	F	152	0[1]
10/10/1999	T	F x 0.7	160	0[1]
10/10/1999	T	F x 1.3	155	220
26/10/1999	T	F x 0.5	190	0[1]
26/10/1999	T	F x 0.9	180	250
05/02/2005	T	F x 1.3	150	0[1]
05/02/2005	T	F x 1.3	155	200

[1] Assumed.

based on the Spencer et al. (2005) and Feaga et al. (2008) distributions. Results on the best fit gas temperatures are given in Table 4.

As shown in Fig. 8 (lower panels), the Spencer et al. (2005) distribution provides a satisfactory match of the IRAM-30 m leading side observations (green line), for a gas temperature of 128 K. On the trailing side, the Spencer et al. (2005) model produces lines at the 20−35 K level as observed using a gas temperature of 136 K, but fails to reproduce the relative line contrasts; specifically, it underpredicts the strong 222 GHz line and overpredicts the weaker 104 GHz and especially 147 GHz transitions. This is indicative of excessive optical depths in the model, and can be corrected by uniformly multiplying the SO_2 columns by a factor of 0.2 ("modified Spencer distribution"). In this case, a gas temperature of 150 K is required to fit the trailing side data (pink line in Fig. 8), although the modeled lines, particularly at 222 GHz and 104 GHz, are too narrow. We address this problem below.

With the original Feaga et al. (2008) distribution, gas temperatures of ∼150 K are required to reproduce the order of magnitude of the line contrasts. These are typically 20 K warmer than inferred from the original Spencer et al. (2005) model. However, on the leading side, the Feaga et al. (2008) distribution now overpredicts the ratio of the strong line to the weak lines (Fig. 9). This indicates insufficient line opacities, i.e. the SO_2 column density is too small. Matching the absolute and relative line contrasts there is achieved by scaling the original SO_2 columns everywhere upwards by a factor ∼3 ("modified Feaga distribution"). On the trailing side, the original Feaga et al. (2008) distribution

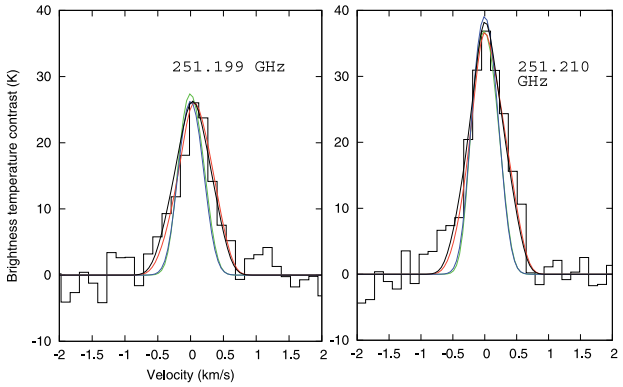

Fig. 10. Fit of IRAM-30 m November 26, 1999 (trail) observations. Data are shown as black histograms. Green: rescaled Spencer distribution. Blue: rescaled Feaga distribution. Red: rescaled Spencer distribution with winds. Black line: rescaled Feaga distribution with winds. See text and Table 4 for details and parameters.

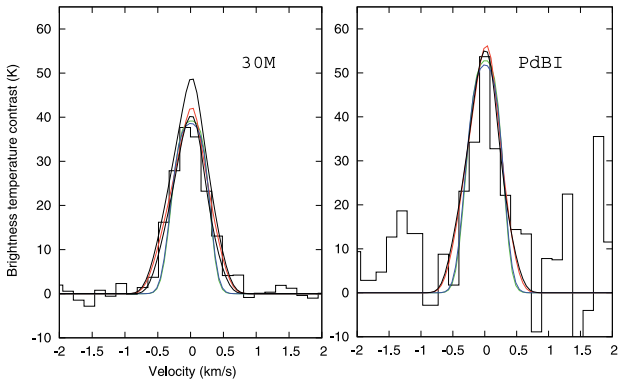

Fig. 11. Fit of 216.643 GHz leading side disk-average spectrum. *Left*: IRAM-30 m (Nov. 25, 1999). *Right*: PdBI (Jan. 28, 2005). Data are shown as black histograms. The spectral resolution is 100 kHz for IRAM 30-m and 120 kHz for PdBI. Green: rescaled Spencer distribution. Blue: rescaled Feaga distribution. Red: rescaled Spencer distribution with winds. Black line: rescaled Feaga distribution with winds. See text and Table 4 for details and parameters.

yields marginally incorrect relative line contrasts, and is then optimally rescaled by a factor of 0.7.

For the Nov. 26, 1999 observations (trailing side), optimum line contrasts were obtained by rescaling the Spencer et al. (2005) and Feaga et al. (2008) distributions by factors of 0.2 and 0.5, generally consistent with the Oct. 10 results. Again in Fig. 10 the synthetic 251 GHz lines are too narrow. Finally, the Nov. 25, 1999 217 GHz observation (leading side), being restricted to one SO_2 line only (216.643 GHz), does not allow one to disentangle between gas temperature and column density effects. It was therefore analyzed with the scaling factors determined from the Oct. 9 observations (Fig. 11). Best fit gas temperatures are gathered in Table 4. Overall, best fit gas temperatures in these models are 128−145 K on the leading side and 150−190 K on the trailing.

As mentioned above, with the modified Spencer et al. (2005) and Feaga et al. (2008) distributions, the synthetic spectra are often too narrow, particularly on the trailing side. This suggests that another broadening factor is playing a role. In the framework of a hydrostatic model, a possible solution is to invoke a horizontal wind.

Sublimation-driven winds are predicted in Io's atmosphere, as a result of pressure gradients. With uniform frost coverage and a surface temperature that decreases smoothly away from the subsolar point, day-to-night winds are expected to occur, with maximum velocity near the terminator of ∼300−350 m/s (Ingersoll et al. 1985; Moreno et al. 1991; Wong & Johnson 1995). We found that this scenario does not provide a satisfactory match of the IRAM-30 m data. Indeed, reproducing the observed trailing side linewidths would require a huge ∼600 m/s day-to-night flow. Moreover, because such a flow appears recessing everywhere on the disk, it would produce strongly redshifted (by about 250 m/s) disk-averaged lines. As shown in Table 3, disk-averaged redshifts do not exceed ∼100 m/s.

An alternate solution is to invoke an atmospheric "superrotation". With projected speeds of opposite sign on the two limbs, this case produces velocity broadening more readily than the day-to-night flow, while maintaining low Doppler shifts on the disk-averaged lines. We found that introducing a 170−300 m/s equatorial zonal velocity allows a considerably improved match of the trailing side linewidths (Figs. 8−10). Such velocities remain consistent with the leading side lines and actually improve the fit of the 217 GHz line (Fig. 11). As horizontal velocities produce extra line smearing, gas temperatures must be somewhat increased (by 2−15 K) to reproduce the observed line contrasts. In some cases, the scaling factor to the SO_2 distribution had to be slightly readjusted. Best fit model parameters are given in Table 4. The linewidths, in themselves, do not allow to distinguish between direct and retrograde winds. The above mentioned 170−300 m/s velocities assume westerlies (direct) winds, as suggested by the Doppler shift map inferred from the PdBI data (Fig. 6). Easterlies (retrograde) winds would have to be 150 m/s stronger, in order to compensate for Io's 75 m/s solid rotation.

For the models presented so far, the unit vertical optical depth is always reached at altitudes lower than 60 km, and in most cases under 30 km. This implies that the above "mean" gas temperatures refer to the lower atmosphere (below 100 km in any case). An alternate means to estimate the mean probed altitude is to consider atmospheres with a vertical thermal gradient. For example, for the Spencer et al. (2005) distribution, the Oct. 9 (leading side) lines can be fit with a 120 K surface temperature and a thermal gradient of 0.25 K/km. Such a profile crosses the isothermal solution (T = 128 K) at 32 km, which thus represents the sounded altitude.

5.3. Fitting the PdBI data

The spatial resolution and signal-to-noise of the PdBI data are insufficient to actually retrieve the spatial distribution of the SO_2 emission. Since these data are also restricted to a single line, our approach is rather to test the two assumed distributions, modified by the scaling factors determined previously from the Oct. 1999 data. For the leading and trailing side respectively, these multiplicative factors are 3 and 1.3 for the Feaga distribution, and 1 and 0.4 for the Spencer distribution. Using constraints from the IRAM-30 m data taken 6 years before is certainly not without risk, especially for the trailing side (where the line contrast appears much lower on the PdBI data than on the 30 m data), but is a reasonable starting approach. The free parameters are again the gas temperature (assumed vertically and horizontally constant) and the velocity field.

On the leading side, the 330 ± 100 m/s limb-to-limb Doppler shift difference (Fig. 6) is best reproduced by a direct flow with 200 ± 70 m/s equatorial velocity, independent of the assumed

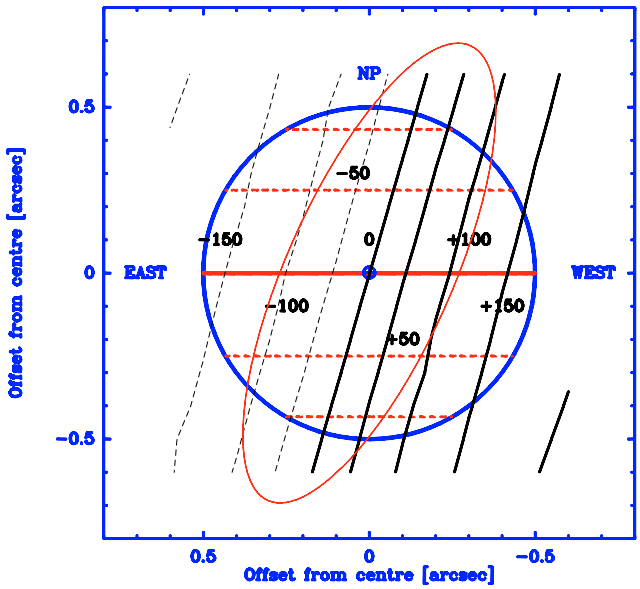

Fig. 12. Doppler shifts for a hydrostatic model with a direct wind speed of 200 m/s.

gas distribution (Fig. 12). This is strikingly similar to the velocity range inferred to match the IRAM-30 m data, supporting the above interpretation of the disk-integrated linewidths. With such a wind, the best fit gas temperature is 166−175 K for the modified Spencer and Feaga cases. On the trailing side, we have no direct evidence for wind, but if one similarly assumes a 200 m/s flow, the derived gas temperature is 155−160 K. We note however that the model, in this simple form (constant gas temperature, constant zonal velocity) predicts only small variations of the linewidths over the disk, from 500 m/s on the west limb to 600 m/s on the east, while a larger range of variation is suggested by the data (from 350 ± 110 to 600 ± 110 m/s).

Analysis of the models in visibility space provides their spatial characteristics (position and width). We performed elliptical fits of the model in the same manner as we did for the data in Sect. 4. Beam orientation was fixed to the value found for the data, so the characteristic sizes of data and models can be directly compared. Results are given in Table 5. All models predict a sky-east (resp. sky-west) displacement of the maximum on the leading (resp. trailing) side, resulting from the maximum amount of SO_2 gas on the anti-jovian hemisphere. On the leading side, the direction of the displacement agrees with the measurement, and its value (≈0.05″) is somewhat smaller. On the trailing side, the predicted sky-west displacement is not observed. On both sides, the (rescaled) Spencer et al. (2005) distribution, being more peaked, yields a somewhat narrower emission size than the Feaga et al. (2008) distribution, in general better agreement with data. For the disk fitting models the Spencer et al. (2005) distribution overpredicts the measured size by 1.0σ and 1.7σ on the leading and trailing side respectively, while the corresponding figures are 1.9σ and 3.5σ for the Feaga et al. (2008) cases. The agreement is slightly better for the Gaussian-fitting models.

A possible way to get a better optimum fit is to further assume that the emission is restricted to a given range of solar zenith angle (SZA). Such a behavior may naturally be expected for a sublimation-driven atmosphere in which the frost has low thermal inertia, and may be also consistent with the HST observations of Jessup et al. (2004), which indicate a steady decrease of the SO_2 columns away from the subsolar point, although it cannot be ascertained whether this behavior reflects

Table 5. Elliptical fits of modeled SO_2 spatial distribution. G stands for elliptical Gaussian model, D for elliptical disk model. S and F stand for the Spencer et al. (2005) and Feaga et al. (2008) SO_2 distribution models.

Hemisphere	Gas model	Gas temperature (K)	Fit type	RA (″)	Dec (″)	Resolved size (″)	Total flux (Jy)
Leading	S	166	D	0.03	–0.01	0.99	0.95
			G	0.04	–0.01	0.68	0.97
Leading	F x 3	175	D	0.045	–0.04	1.06	0.94
			G	0.06	–0.04	0.72	0.96
Leading	S*	170	D	0.058	0.00	0.92	0.98
			G	0.06	0.00	0.62	1.00
Leading	S **	180	D	0.066	0.00	0.84	0.94
			G	0.066	0	0.56	0.95
Trailing	S x 0.4	160	D	–0.14	0.01	0.88	0.51
			G	–0.15	0.02	0.61	0.52
Trailing	F x 1.3	155	D	–0.05	0.03	1.11	0.47
			G	–0.08	0.03	0.76	0.48
Trailing	(S x 0.4)**	180	D	–0.08	0.00	0.78	0.48
			G	–0.09	0.00	0.52	0.49
Trailing	(S x 0.4)***	210	D	–0.06	0.00	0.70	0.45
			G	–0.06	0.00	0.46	0.46

* Indicates a distribution restricted to SZA < 70°. ** Indicates a distribution restricted to SZA < 60°. *** Indicates a distribution restricted to SZA < 50°. Ellipse orientation is fixed to the data fit value (−16° for the leading, −6° for the trailing).

variation with latitude or with SZA. To illustrate this, we include in Table 5 a few cases using the (rescaled) Spencer et al. (2005) distribution, but specifying zero emission when the SZA is larger than 70°, 60° or 50°. These restricted models require an increase of the gas temperature to match the observed total flux.

On the leading side, models with an emission limit at SZA 60°−70° allow a good match of the observed emission size. Synthetic images for various models are shown in Fig. 13 for the leading side. Note that since the observations were obtained with a 10° phase angle w.r.t. the sun, the effect of restricting the emission with a SZA range is not symmetric between east and west. The result is a slight displacement of the position of the maximum towards sky east, further improving the match with the observed maximum. On the trailing side, a limiting SZA of 50° on the modified Spencer et al. (2005) distribution provides a good agreement on the emission size. With such a model, the predicted RA position of the maximum is −0.06″, still 1.6σ away from the measured value (+0.02 ± 0.05″).

We note finally that with such "restricted" distributions, accounting for the 330 ± 100 m/s limb-to-limb velocity difference requires an increase of the equatorial wind velocity, by about 50% for a cutoff at 60° SZA, above the 200 ± 70 m/s values previously found. Increased velocities are also required to fit the linewidths of the IRAM-30 m data with the restricted models, as well as increased gas temperatures to account for line contrast. As discussed later, however, the confinement of the atmosphere in the 2005 data does not necessarily hold for the 1999 observations, so we did not perform detailed fits.

6. Contribution of volcanic plumes

Volcanic plumes, one of the most spectacular expressions of volcanic activity on Io, have been observed and monitored since they were discovered in 1979 by Voyager (see review in Geissler & Goldstein 2006). In addition to particles, there is evidence that the erupting volcanic plumes carry out gas. This is based on nighttime and eclipse images of Io auroral glows, which appear to be brighter in the equatorial region and enhanced in the vicinity of volcanic plumes, due to excitation of atmospheric gases by charged particles (Geissler et al. 1999, 2001, 2004b). Also, gaseous SO_2 and S_2 were detected in the Pele plume, resolved by HST against Jupiter (Spencer et al. 2000), and local increases of SO_2 column densities were measured over Pele and Prometheus plume sites by McGrath et al. (2000) and Jessup et al. (2004) respectively.

Ballester et al. (1994) pointed out that the SO_2 linewidths are comparable to the typical ejection speeds and may therefore represent velocity dispersion within erupting plumes. Lellouch (1996) attempted to model the disk-averaged millimeter observations with a highly idealized (purely ballistic and isothermal at T = 250 K) plume model and found that such a model required the simultaneous emission from a large number of plumes – typically 30 on Io's leading side and twice more on the trailing side – erupting at 0.5−0.7 km s^{-1}. In a different but perhaps equally crude approach, Strobel & Wolven (2001) estimated the number of volcanic plumes required to explain the mean equatorial pressure determined from the Ly α observations. Not surprisingly, the result was extremely sensitive to the assumed eruption conditions, ranging from 8 plumes for an ejection velocity v = 1.3 km s^{-1} to 66 plumes for v = 0.75 km s^{-1} and 185 for v = 0.58 km s^{-1}, in general agreement with the previous results.

Neither of these models included a realistic description of the complex physical processes occurring in volcanic plumes. Detailed plume models are now available (Zhang et al. 2003, 2004), which use a direct simulation Monte Carlo (DSMC) approach and include most of the relevant physical effects for proper modeling of the rarefied nature of the gas flow: vent properties, rotational and vibrational radiation and cooling, ballistics, collisions and shocks, sublimation and condensation, plasma heating. Model parameters are the vent characteristics (vent radius, temperature, density and velocity at the vent), the plasma energy flux, and the surface temperature. The latter parameter is crucial for defining the overall plume structure. In night conditions (T_{surf} = 90 K), the gas expands, radiates, and rises until a canopy shock forms due to gravity; it then falls and condenses on the cold ground. While the gas temperature above the vent decreases to very low temperatures (e.g. T = 50 K) due to plume expansion and vibrational cooling, the gas temperature in the canopy shock reaches 300−400 K. In day conditions (T_{surf} = 115 K in Zhang et al. 2003 and 110−118 K in Zhang et al. 2004)

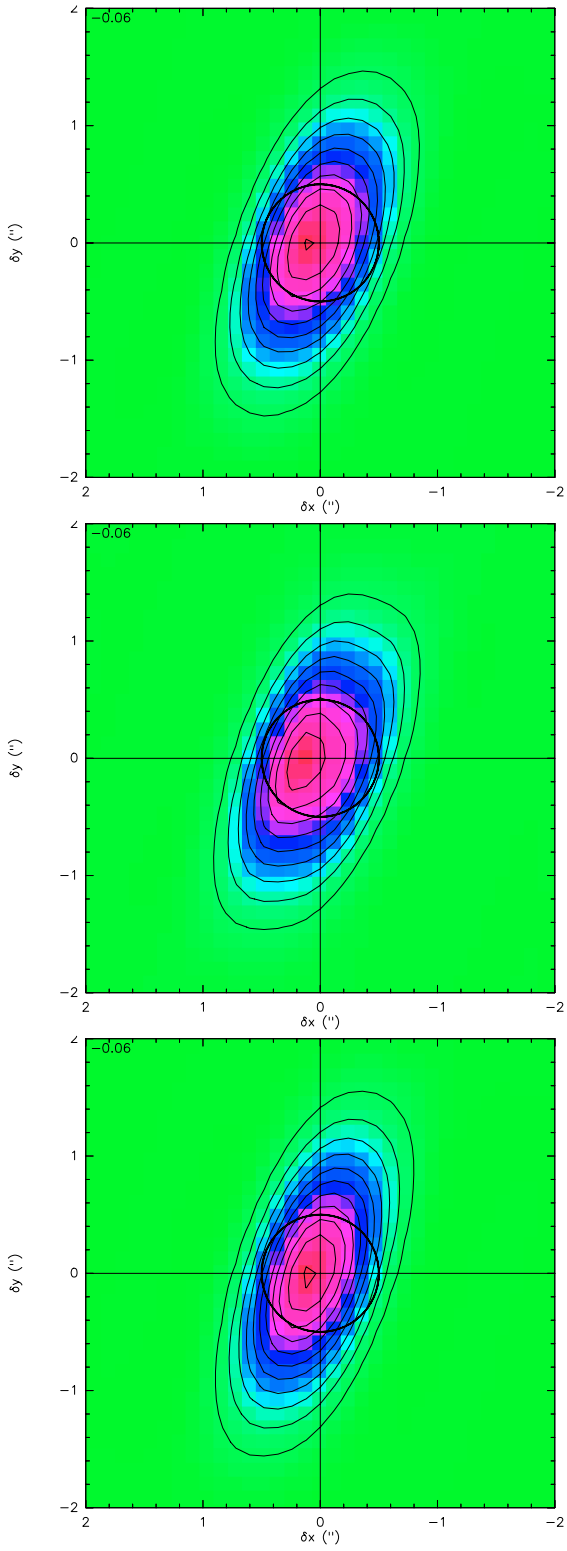

Fig. 13. Model emission maps on the leading side. *Top*: rescaled Spencer distribution, *Center*: rescaled Feaga distribution, *Bottom*: rescaled Spencer distribution, restricted to SZA < 70°. Gas temperature is adjusted so as to reproduce the observed total flux (see Table 5). Contour step is 50 mJy/beam.

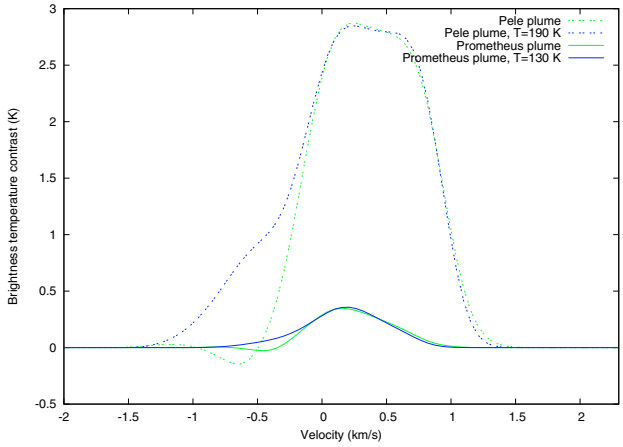

Fig. 14. 217 GHz emission line, rescaled to Io radius, produced by 1 nightside Pele or Prometheus plume located 40° away from disk center. Assumed fluxes are 2×10^{29} and 1.1×10^{29} SO_2 molecules s^{-1}, respectively. Also shown are synthetic spectra calculated for isothermal plumes.

and if frost is present in the plume vicinity, the falling plume bounces on a sublimation layer, producing one (or more) reentry shock(s) with ~300 K gas temperature, and partly eroding the background atmosphere. Zhang et al. (2003) modeled both the large Pele- and smaller Prometheus-type plumes (as defined in the classification of McEwen & Soderblom 1983), using appropriate ejection velocities (resp. 0.9 and 0.5 km s^{-1}) and vent temperatures (resp. 650 and 300 K). Due to multiple bounces, dayside plumes are several (2–5) times broader than their nightside counterparts. The dayside case may be more relevant for Prometheus than for Pele as Prometheus-type plumes appear to form from the interaction of lava flows with a SO_2-rich surface, while Pele seems to directly exhale sulfur-rich gases from Io's interior (Milazzo et al. 2001; Radebaugh et al. 2004).

We adapted the Zhang et al. (2003) models to investigate the plausible contribution of volcanic plumes to the SO_2 millimeter emission. We used a vent radius of 8.6 km and a vent density of 1×10^{18} m^{-3}. This corresponds to a flux of 2×10^{29} (resp. 1.1×10^{29}) SO_2 molecules s^{-1} for the Pele and Prometheus cases, i.e. mass fluxes of 2.1×10^4 kg s^{-1} and 1.1×10^4 kg s^{-1} respectively. These fluxes are chosen so that the plume-averaged column densities (over 450 km radius for Pele and 200 km radius for Prometheus) match the observations of Spencer et al. (2000) at the Pele site (about 3.5×10^{16} cm^{-2}, when converted to vertical viewing) and of Jessup et al. (2004) for the "excess SO_2" over the Prometheus site (5×10^{16} cm^{-2}). The plume model was incorporated in a radiative transfer model with a 20 km resolution grid. We focused on night-side plumes, which essentially represent the limiting case of a "purely volcanic" atmosphere. Figure 14 shows computations of the 217 GHz line for a single night-side (Pele or Prometheus) plume, located on the equator 40° away from disk center. With the adopted SO_2 gas flux, the brightness temperature contrast (scaled to Io radius) is 0.3 K for the Prometheus case, and 3.1 K for the Pele cases. Lines are overall redshifted by ~0.23 km s^{-1} (Prometheus) and ~0.38 km s^{-1} (Pele), reflecting the gas falling away from the observer. Lines also exhibit a small blueshifted absorption, due to the cold rising plume core a few tens of km above the vent. Linewidths are about 0.96 km s^{-1} for Pele and 0.68 km s^{-1} for Prometheus. For comparison, Fig. 14 also shows that to first order the flux emitted in the Pele plume is the same as that of an isothermal plume at $T \sim 190$ K, while the mean emitting temperature of Prometheus is ~130 K.

With the above values, the observed line contrasts, if resulting from a purely volcanic atmosphere, would require emission from typically ~100 (Prometheus) or 15 (Pele) plumes on the

leading hemisphere, and maybe half of this on the trailing. This exceeds the number of actually observed plumes (18 in total, including only half-a-dozen large ones Geissler et al. 2004a) by a large factor. Given also that the Prometheus case matches the linewidths, the conclusions of Lellouch (1996) and Strobel & Wolven (2001) on the large number of plumes required and the appropriate ejection velocity range needed are put on much firmer ground. To account for the difference between the required and actually observed plumes, Johnson et al. (1995) postulated the existence of "stealth plumes", i.e. plumes without entrained particulates. We note however, that the general association of enhanced auroral glows with visible plume location tends to argue against the existence of widespread stealth plumes; the only well-characterized exception seems to be Acala (Geissler et al. 2001).

In summary, we believe this demonstrates that an atmosphere restricted to the quasi-ballistic plume centers cannot explain the observations. We briefly considered the case of dayside plumes. Zhang et al. (2004) showed that their "Prometheus day" plume models with entrained nanometer-size dust particles can reproduce the detailed structure of the visible Prometheus plume, including the shadow it casts on the ground up to several hundreds of kilometers from plume core. Using a standard 112 K surface temperature, we calculated the contribution of a single dayside Prometheus plume over a 600 km radius, the range covered by the plume model. With such a surface temperature, the sublimation component is 2.6×10^{16} cm^{-2}. The brightness temperature contrast produced by such a plume at the center of the disk, scaled to Io's radius, is now 9 K. The required number of such plumes is then drastically reduced, making the case plausible. However, emission in that case is dominated by the sublimation component (due to its broader extension), which is highly sensitive to surface temperature. Averaged over the plume radius (200 km and 450 km for Prometheus and Pele), the brightness temperature contrast is only 40 K and 65 K for the Prometheus and Pele cases. This is comparable to the ∼25−60 K mean brightness temperature contrasts in the emitting region, as determined from the PdBI data. Therefore, the dayside plume case is not easily distinguished from the hydrostatic atmosphere envisaged earlier, and even in highly spatially resolved emissions, plume centers may actually not stand out strongly above (or below) the "background" level. In addition, the 600 km dimension appears to be an artificial limit, and the extent of dayside plume atmospheres is in fact defined by the presence/absence of surface frosts and by the surface temperature variation across Io's dayside. To test dayside volcanic plume models in a fully realistic manner, a complete model of the whole Io atmosphere with DSMC, including a distribution of volcanic sources, frosts, and surface temperatures, would be needed in the first place.

7. Discussion

In spite of their modest spatial resolution and S/N ratio, these first disk-resolved millimeter observations of Io's atmosphere, combined with a reanalysis of high-quality IRAM-30 m data in the light of newly proposed SO_2 distributions and volcanic plume models, suggest a picture rather different from the one based on the early IRAM-30 m observations. In the framework of a hydrostatic atmosphere model, the initial interpretation of the disk-integrated spectra used the line widths, absolute and relative contrasts to deduce the SO_2 mean column densities, gas temperature, and fraction of the projected surface (f_p) covered by the atmosphere. For observations gathered in 1991−1994, this approach indicated a very localized and hot atmosphere (f_p = 5−8% and T = 500−600 K on the trailing side, f_p = 12−16% and T = 250−400 K on the leading side). Data from 1999 pointed to a more extended and somewhat cooler atmosphere, covering ∼15% (trailing) – 42% (leading) of the projected disk, with gas temperatures of about 400 K and 200 K respectively (McGrath et al. 2004; Lellouch et al. 2006).

In the current (still hydrostatic) analysis of the 1999 disk-averaged data, the gas distribution is a priori assumed (i.e., the f_p factor is no longer relevant). Although a scaling factor on the gas densities is determined from the relative line contrasts, the gas temperature is now essentially measured from the absolute line contrasts. The inferred gas temperatures are low (<200 K), and an adequate fit of the linewidths is achieved by introducing horizontal velocities at the 170−300 m/s level. Doppler shifts measured from PdBI in 2005 directly reveal that such planetary-scale gas velocities are present on Io's leading side.

The atmospheric coverage indicated by the PdBI data in 2005 (45−75% and 75−90% on the trailing and leading side, respectively) is considerably larger than the initial estimates based on the IRAM-30 m data only. Still, it is smaller, particularly on the trailing side, than one would expect based on SO_2 distributions proposed from UV imaging and thermal IR observations. Reconciliation is possible by restricting these distributions to a given SZA range, typically 60°. This, and the insufficient number of volcanic plumes, point to a dominantly sublimation-controlled atmosphere. Similarly, from comparing the dayside and nightside auroral glows observed by New Horizons/ Alice UV spectrometer, Retherford et al. (2007) also concluded that the contribution of volcanic plumes is minor on the dayside.

Gas temperatures determined from the various observations and models span the range 130−210 K. Compared to the initial analysis, these lower gas temperatures are a direct consequence of the larger spatial extent. The multiple line IRAM-30 m 1999 observations allow the most reliable determination of the mean gas temperature, and point to warmer temperatures on the trailing side (160−185 K) than on the leading (128−145 K). These values are based on the linearly modified SO_2 distributions. As already mentioned, we did not attempt to refit the 1999 data with SZA restricted models. On the trailing side, the factor-of-2 lower line fluxes in 2005 compared to 1999 points to a large temporal variation. Its origin is uncertain but, for a sublimation-driven atmosphere, it could conceivably be due to the variation of Io's heliocentric distance (4.96 AU in 1999 vs. 5.45 AU in 2005 and in 1993−1994). To first order, this could cause a decrease of the surface temperatures by ∼5 K, with attendant shrinking of its lateral extent from 1999 to 2005. If the actual SO_2 distribution in 1999 is more localized than assumed, these derived gas temperatures would be lower limits. For nominal atmospheric coverages of ∼80% and 55%, the required temperatures would roughly increase by ∼10 K on the leading side and ∼60 K on the trailing side, further increasing the trail-to-lead temperature difference. In light of the Strobel et al. (1994) 1-D and Wong & Smyth (2000) 2-D models, a warmer trailing side atmosphere is not surprising given its lower column densities and the likely contribution from the plasma flow there.

The cool gas temperatures that we infer now are in line with those inferred from other techniques. While UV spectra are only weakly gas temperature-dependent, the highest-quality spectra of Jessup et al. (2004) indicate gas temperatures in the range 150−250 K. In the thermal range, the Spencer et al. (2005) observations provide a stringent T < 140−150 K upper limit on the gas temperature, at least on the anti-jovian hemisphere where the SO_2 19 μm absorption bands are deepest. For observations centered at 90° and 270°, the gas temperature constraint can be

relaxed to $T < 170$ K and $T < 190$ K (see Fig. 16 of Spencer et al. 2005).

The SO_2 amounts we derive are reassuringly intermediate between those of the Feaga et al. (2008) and Spencer et al. (2005) distributions, which typically differ by a factor of 3. Tracking down the sources of the remaining differences is not easy. For example, there is no obvious explanation why the Spencer et al. (2005) distribution matches the IRAM-30 m data on the leading side, but must be scaled down by a factor of 2.5 to match the trailing side observations. Regarding the Feaga et al. (2008) distribution, we find it necessary to scale it upwards by a factor 3 on the leading side. Yet, formal error bars on the SO_2 columns as derived from the HST Lyα images are estimated to be typically 30%, and at most a factor of 2 on some pixels in the anti-jovian hemisphere (Feaga et al. 2008; L. Feaga, priv. comm.). A possible way of reconciliation would be to assume that the atmospheric columns vary on spatial scales smaller than the ~200 km resolution of the HST imaging, with dense patches saturating out the Ly α absorption.

One of the most important results of our observations is the detection of a 330 ± 100 m/s limb-to-limb difference in the leading side line Doppler shifts. To first order, this can be modeled by means of a direct zonal flow from West to East. This is puzzling as models (e.g. Ingersoll et al. 1985; Ingersoll 1989) have predicted for a long time a primarily day-to-night circulation which for uniform frost coverage should be seen as identical Doppler shifts on the two limbs. Still, the wind regime may be strongly modified in the presence of geographical (and not only diurnal) variations of the surface pressure. As winds blow from dense to tenuous regions, the observed wind direction on the leading side may result from the ~10 times larger SO_2 densities on the anti-jovian hemisphere. Dayside Prometheus plume models (Zhang et al. 2003) show large horizontal velocities (Mach number ~3, i.e. ~300 m/s) several hundred kilometers away from the plume core. The approaching winds we see on the east limb may conceivably result from the presence of several plumes (Prometheus, Culann, Zamama, Volund, and Marduk) on this part of the disk for the leading side observations, although as mentioned above, we are not able to test this idea quantitatively. If this interpretation is valid, apparently retrograde winds should be observed on the trailing side. Another mechanism possibly producing Doppler shifts is angular momentum transfer from the plasma flow hitting Io's trailing side at 57 km s^{-1} relative velocity. Evidence for drag forces from the ion torus interaction is given by Saur et al. (2002). These forces can set the gas into motion, qualitatively explaining the sign of the disk-averaged Doppler shifts (Table 3). However, this mechanism is expected to result in blueshifts everywhere on the leading side. A combination of plasma momentum transfer and day-to-night flow would thus have to be invoked, each of them dominating on a different limb. We recognize that these considerations remain qualitative, and have no satisfactory explanation. Additional observations, at improved spatial resolution and signal-to-noise, and including multiple lines, are required. Similar observations have been obtained with the Submillimeter Array (SMA) in June 2006 (Gurwell et al. 2007) and will be published elsewhere. In the reasonably close future, observations with ALMA at ~0.1″ spatial resolution will be invaluable to sort out the complex behavior of Io's atmosphere.

Acknowledgements. We thank the IRAM Director for allocating Discretionary Time and the Plateau de Bure Interferometer staff for performing the observations. We thank William Thuillot (IMCCE) for providing us with the Io ephemeris for velocity corrections, and Lori Feaga for providing us with a digitized version of her SO_2 distribution map.

References

Austin, J. V., & Goldstein, D. B. 2000, Icarus, 148, 370
Ballester, G. E., McGrath, M. A., Strobel, D. F., et al. 1994, Icarus, 111, 2
De Pater, I., Brown, R. A., & Dickel, J. R. 1984, Icarus, 57, 93
Domingue, D. L., Lockwood, G. W., & Kubala, A. E. 1998, Icarus, 134, 113
Douté, S., Schmitt, B., Lopes-Gautier, R., et al. 2001, Icarus, 149, 107
Emery, J. P., Sprague, A. L., Witteborn, F. C., et al. 1998, Icarus, 136, 104
Feaga, L. M. 2005, BAAS, 37, 764
Feaga, L. M., McGrath, M. A., & Feldman, P. D. 2008, Icarus, submitted
Geissler, P. E., & Goldstein, D. B. 2006, Plumes and their deposits, in Io after Galileo (Springer), 164
Geissler, P. E., McEwen, A. S., Ip, W., et al. 1999, Science, 285, 870
Geissler, P. E., Smyth, W. H., McEwen, A. S., et al. 2001, JGR, 106, 26137
Geissler, P., McEwen, A., Phillips, C., Keszthelyi, L., & Spencer, J. 2004a, Icarus, 169, 29
Geissler, P., McEwen, A., Porco, C., et al. 2004b, Icarus, 172, 127
Guilloteau, S., Delannoy, J., Downes, D., et al. 1992, A&A, 262, 624
Gurwell, M. A., Moullet, A., Lellouch, E., & Moreno, R. 2007, in AAS/Division for Planetary Sciences Meeting Abstracts, 39, 03.04
Hogbom, J. A., & Brouw, W. N. 1974, A&A, 33, 289
Ingersoll, A. P. 1989, Icarus, 81, 298
Ingersoll, A. P., Summers, M. E., & Schlipf, S. G. 1985, Icarus, 64, 375
Jessup, K. L., Spencer, J. R., Ballester, G. E., et al. 2004, Icarus, 169, 197
Johnson, T. V., Matson, D. L., Blaney, D. L., Veeder, G. J., & Davies, A. 1995, GRL, 22, 3293
Kerton, C. R., Fanale, F. P., & Salvail, J. R. 1996, JGR, 101, 7555
Laver, C., de Pater, I., Roe, H., & Strobel, D. F. 2007, Icarus, 189, 401
Lellouch, E. 1996, Icarus, 124, 1
Lellouch, E., Belton, M., de Pater, I., et al. 1992, Icarus, 98, 271
Lellouch, E., Strobel, D. F., Belton, M. J. S., et al. 1996, ApJ, 459, L107
Lellouch, E., McGrath, M. A., & Jessup, K. L. 2006, Io's atmosphere, in Io after Galileo (Springer), 231
McEwen, A. S. 1988, Icarus, 73, 385
McEwen, A. S., & Soderblom, L. A. 1983, Icarus, 55, 191
McGrath, M. A., Belton, M. J. S., Spencer, J. R., & Sartoretti, P. 2000, Icarus, 146, 476
McGrath, M. A., Lellouch, E., Strobel, D. F., Feldman, P. D., & Johnson, R. E. 2004, Satellite atmospheres, in Jupiter. The Planet, Satellites and Magnetosphere (Cambridge University Press), 457
Milazzo, M. P., Keszthelyi, L. P., & McEwen, A. S. 2001, JGR, 106, 33121
Mitchell, D. L., & de Pater, I. 1994, Icarus, 110, 2
Moreno, M. A., Schubert, G., Kivelson, M. G., Paige, D. A., & Baumgardner, J. 1991, Icarus, 93, 63
Moreno, R., Marten, A., & Hidayat, T. 2005, A&A, 437, 319
Muhleman, D. O., & Berge, G. L. 1991, Icarus, 92, 263
Pickett, R. L., Poynter, E. A., Cohen, E. A., et al. 1998, J. Quant. Spectrosc. Radiat. Transf., 60, 883
Radebaugh, J., McEwen, A. S., Milazzo, M. P., et al. 2004, Icarus, 169, 65
Retherford, K. D., Spencer, J. R., Stern, S. A., et al. 2007, in AAS/Division for Planetary Sciences Meeting Abstracts, 39, 15.04
Rudy, D. J., Muhleman, D. O., Berge, G. L., Jakosky, B. M., & Christensen, P. R. 1987, Icarus, 71, 159
Saur, J., & Strobel, D. F. 2004, Icarus, 171, 411
Saur, J., Neubauer, F. M., Strobel, D. F., & Summers, M. E. 2002, JGR, 107, 5
Simonelli, D. P., Veverka, J., Senske, D. A., et al. 1998, Icarus, 135, 166
Simonelli, D. P., Dodd, C., & Veverka, J. 2001, JGR, 106, 33241
Smyth, W. H., & Wong, M. C. 2004, Icarus, 171, 171
Spencer, J. R. 1990, Icarus, 83, 27
Spencer, J. R., Lebofsky, L. A., & Sykes, M. V. 1989, Icarus, 78, 337
Spencer, J. R., Jessup, K. L., McGrath, M. A., Ballester, G. E., & Yelle, R. 2000, Science, 288, 1208
Spencer, J. R., Lellouch, E., Richter, M. J., et al. 2005, Icarus, 176, 283
Strobel, D. F., & Wolven, B. C. 2001, APSS, 277, 271
Strobel, D. F., Zhu, X., & Summers, M. F. 1994, Icarus, 111, 18
Veeder, G. J., Matson, D. L., Johnson, T. V., Blaney, D. L., & Goguen, J. D. 1994, JGR, 99, 17095
Vogler, K. J., Johnson, P. E., & Shorthill, R. W. 1991, Icarus, 92, 80
Winter, D. F., & Krupp, J. A. 1971, Moon, 2, 279
Wong, M. C., & Johnson, R. E. 1995, Icarus, 115, 109
Wong, M. C., & Johnson, R. E. 1996, JGR, 101, 23243
Wong, M. C., & Smyth, W. H. 2000, Icarus, 146, 60
Zhang, J., Goldstein, D. B., Varghese, P. L., et al. 2003, Icarus, 163, 182
Zhang, J., Goldstein, D. B., Varghese, P. L., et al. 2004, Icarus, 172, 479
Zolotov, M. Y., & Fegley, B. 1998, Icarus, 133, 293

Table A.1. Physical observation parameters of flux calibrators.

Target	Date	Observed CML (° W)	Apparent diameter (″)
Callisto	28/01/2005	262–267	1.312
Callisto	05/02/2005	74–80	1.344
Ganymede	28/01/2005	45–60	1.438
Ganymede	05/02/2005	90–100	1.472

Appendix A: Absolute flux calibration

We chose to use Galilean satellites Callisto and Ganymede to assess the absolute flux scale. As a first step, we determined total continuum fluxes and equivalent brightness temperatures on each of the bodies and each of the observing dates. For this task, we assumed uniform brightness temperature disks of the appropriate sizes (see Table A.1). The data were then self-calibrated in phase, and the visibilities in the u, v plane were fit with a circular and uniform brightness disk model, with the total flux as the free parameter. For each object and date, the total flux was converted to a mean equivalent brightness temperature T_B. Total fluxes and brightness temperatures were then corrected by a calibration factor, adjusted to yield T_B = 95 K for Ganymede's leading side at 1.4 mm. This value is taken from well-calibrated measurements obtained at the Submillimeter Array (SMA) in June 2006 and at PdBI in May 2006 by two of us (M. A. Gurwell and R. Moreno, respectively; data to be published elsewhere), and bears an estimated uncertainty of 5%. The same calibration factor yielded T_B = 119 K for Callisto (both sides), within 1% of the value determined from SMA observations. With this calibration, we determined for Io a mean 1.4 mm brightness temperature of 93 K on the leading side and 99 K on the trailing side. At 3 mm, the same approach, using for calibration T_B = 85.5 K for Ganymede's leading side, yielded T_B = 96 K and 100 K for Io's leading and trailing side, respectively. These values agree with the 1.4 mm brightness temperatures within the 5% absolute uncertainty. In addition, the same procedure gave T_B = 111 K at 3 mm for Callisto. This agrees to within ∼3% with the PdBI May 2006 measurements, which gives T_B = 108 K (in other words, at 3 mm, our observations give a Callisto/Ganymede ratio higher by just ∼3% compared to the other measurements), giving confidence in the calibration method.